

## **Annex 1**

# **Numerical simulation of the flow situation in an experimental device for emulsification**

Part of the CONEX-Project  
**Emulsions with Nanoparticles for New Materials**



Institut für Strömungslehre und Wärmeübertragung  
Technische Universität Graz

Mag. Dr. techn. Renate Teppner  
Ass.-Prof. Dipl.-Ing. Dr. techn. Helfried Steiner  
O. Univ.-Prof. Dr.-Ing. habil. Günter Brenn

Graz, October 2004

# Contents

1. Computed flow configuration - geometry	3
2. Parameters for the numerical simulation	5
2.1. Boundary conditions	5
2.2. Numerical scheme	6
3. Results of the simulation	7
4. Estimation of the maximum droplet size based on the numerical results	17
4.1 Comparison with experimental data	19
5. Discussion and further work	22
6. Emulsification by liquid jet break-up in another viscous fluid	21
References	25

## Formal aspects of the project

After finalisation of all formal procedures for establishing the project “EMMA” – Emulsions with Nanoparticles for new Materials, the project started on October 20, 2003. The project is run by three partners – the Institute of Fluid Mechanics and Heat Transfer (ISW) of Graz University of Technology, Graz (Austria), the Laboratory of Chemical Physics and Engineering (LCPE) of the University of Sofia (Bulgaria), and the Department of Mechanics and Physics of Fluids (DMPF) of the Polish Academy of Sciences, Warsaw (Poland).

The kick-off meeting took place at the LCPE in Sofia between Friday, October 31 and Sunday, November 2, 2003. In this meeting, all partners presented their institutions and fields of work. Specific presentations related to the EMMA project were also given by all three partners, where the group from LCPE presented very interesting results of preliminary investigations in the field of emulsification in the presence of surfactants at various concentrations. The essential question there is the population of drops of the disperse phase and its change due to the emulsification process.

The partners agreed upon having a second meeting for mid-term reporting in October 2004 in Warsaw (Poland). In between the PhD student Slavka Tcholakova from LCPE made a visit to the DMPF in Warsaw for experiments in the field of emulsification in a narrow-gap emulsifier, and a visit of Prof. K. Danov from LCPE to ISW in Graz is planned for the week between December 4 and 10, 2004.

## 1 Computed flow configuration - geometry

According to the geometry data provided by Mrs. Slavka Tcholakova the key part of the emulsifier was constructed as shown in Figure 1. The total axial extension of the computational domain is  $L=0.5$  m. The diameter at the inlet is  $D=0.013$  m.

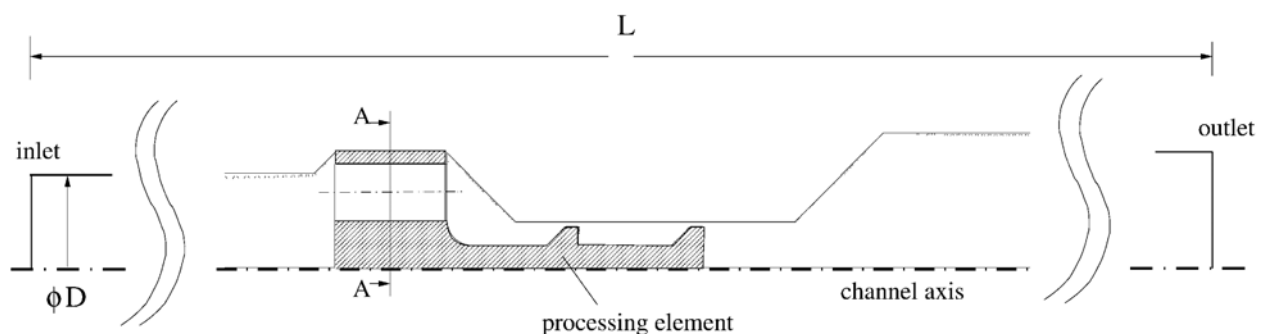


Figure 1: Configuration of the emulsifier.

As it is shown by the cross-sectional view in Figure 2, the processing element's base plate containing six inlet holes exhibits 12 axes of symmetry with respect to the circumferential direction  $\theta$ . Therefore, the present three-dimensional simulation considered a flow geometry bounded by two neighbouring axes of symmetry. As marked by the shaded slice in Figure 2, the computed flow domain has a circumferential extension of  $\Delta\theta = 30^\circ$ .

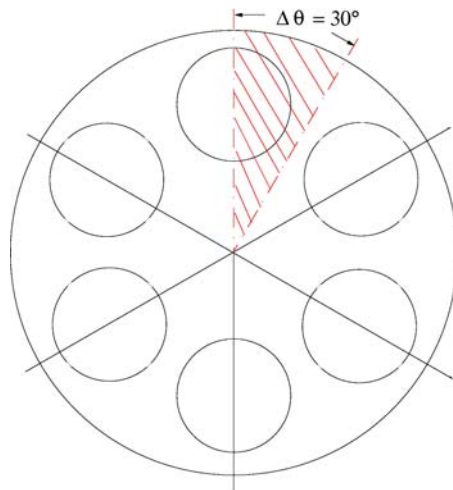


Figure 2: Cross section A-A of the base plate as denoted in Figure 1. The extension of the computational domain in the circumferential direction is  $\Delta\theta = 30^\circ$ .

Figures 3 and 4 display different views of the flow geometry next to the processing element. The gap width is  $395\ \mu\text{m}$ .

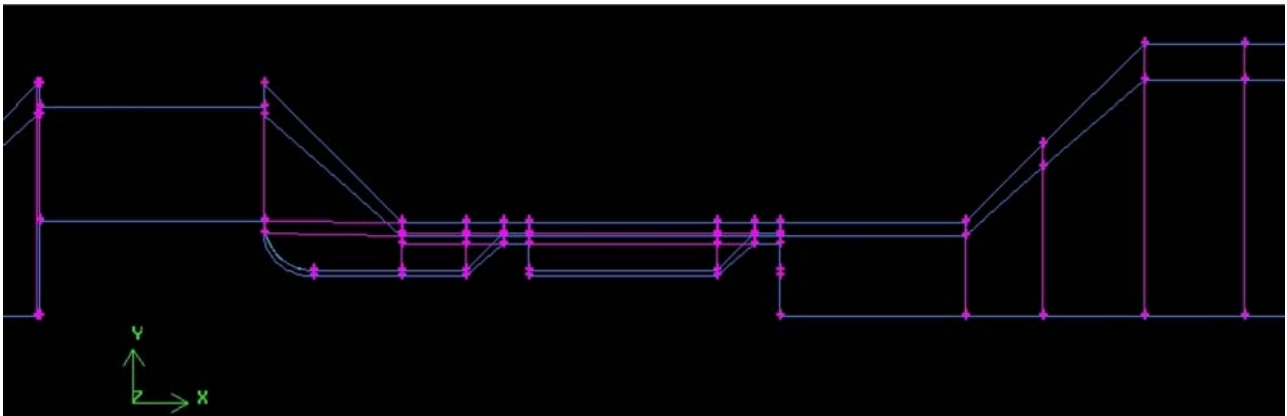


Figure 3: Processing element, gap width  $395\ \mu\text{m}$ .

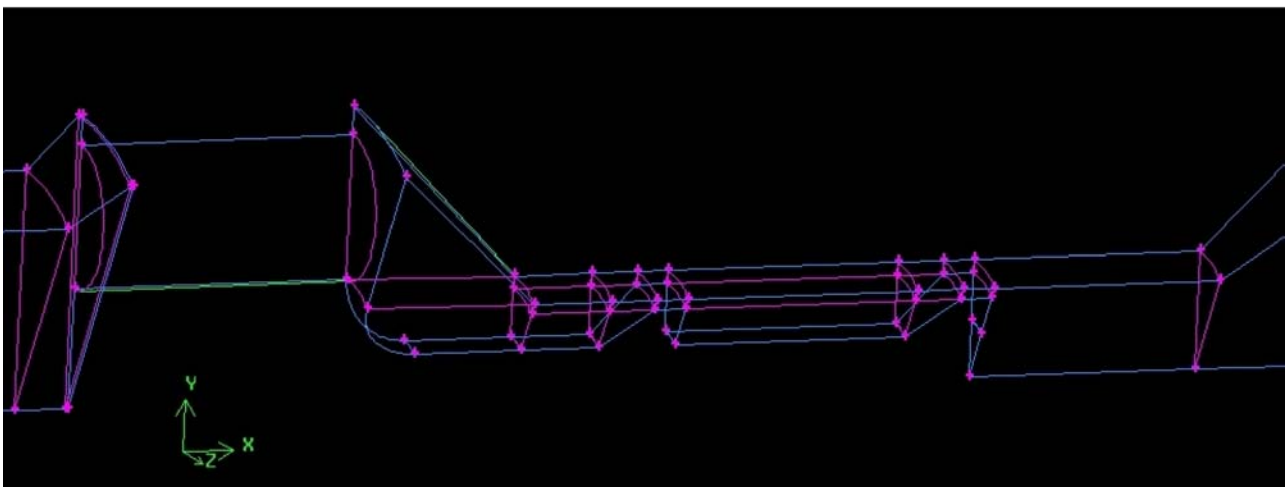


Figure 4: Processing element, gap width  $395\ \mu\text{m}$ .

## 2 Parameters for the numerical simulation

The three-dimensional numerical calculations were done with Fluent 6.1.22. For comparison three different  $k-\varepsilon$  models (Standard, RNG, Realizable) with enhanced wall treatment were used as turbulence models. Applying the alternative turbulence models did not produce significantly different solutions, as it will be shown in the numerical results.

For the material properties of the working fluid we used the corresponding data of the emulsion, which read  $\rho = 977.6 \text{ kg/m}^3$  and  $\mu = 2.5 \cdot 10^{-3} \text{ Pa s}$ , respectively. The volumetric flow rate through the emulsifier was set to  $\dot{V} = 0.13 \cdot 10^{-3} \text{ m}^3/\text{s}$ .

### 2.1 Boundary conditions

The boundary conditions which were imposed at the different boundary zones shown in Figure 5 are summarized in Table 1.

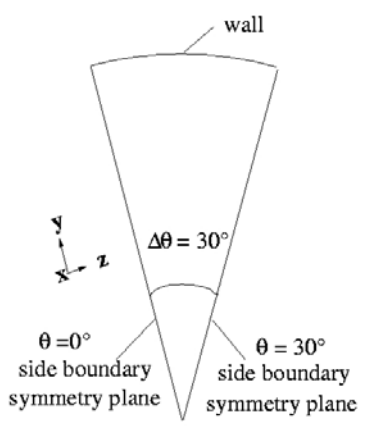
velocity-inlet	inlet velocity: top-hat profile with the axial velocity $v_x = 0.979 \text{ m/s}$ and turbulence intensity 10%, the corresponding Reynolds number based on the diameter at the inlet $D = 0.013 \text{ m}$ is $Re = v_x D \rho / \mu = 4979$
pressure-outlet	von Neumann condition for velocity
channel wall surface of processing element	no slip condition no slip condition
planar side boundaries	<p style="text-align: center;">symmetry</p> 

Table 1: Boundary conditions.

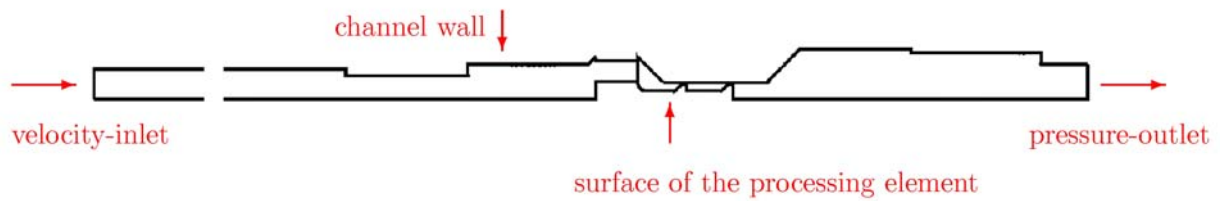


Figure 5: Boundary conditions. At the side boundaries of the domain, i.e., at  $\theta = 0^\circ$  and  $\theta = 30^\circ$ , respectively, the symmetry condition with respect to the circumferential direction  $\theta$  was imposed.

## 2.2 Numerical scheme

The governing set of equations was numerically solved using the following solvers for the pressure field and discretization schemes:

Pressure	Standard
Pressure-Velocity Coupling	SIMPLE
Momentum	First Order Upwind (Standard, RNG), Second Order Upwind (Realizable)
Turbulent Kinetic Energy	First Order Upwind (Standard, RNG), Second Order Upwind (Realizable)
Turbulent Dissipation Rate	First Order Upwind (Standard, RNG), Second Order Upwind (Realizable)

Table 2: Pressure solvers and discretization schemes

## 3 Results of the simulation

The presented results in the area of the processing element are organized as follows:

- Fig. 6 Velocity-vector plot demonstrating the local direction of the flow particularly in the region close to the processing element.
- Figs. 7 - 8 Contour plots of the axial velocity and the static pressure at different cross-sectional (y-z)-planes downstream from the device. These contour plots are shown to illustrate that the flow after passing through the inlet holes of the processing element's base plate becomes again homogeneous in the circumferential direction very rapidly. This is due to the strong contraction of the flow as it approaches the first narrow gap. Therefore, the flow downstream from the first gap of the processing element can be practically regarded as cylindrically symmetric.
- Figs. 9 - 11 Contour plots of the axial velocity component (streamwise direction), of the turbulent kinetic energy, and of the turbulent dissipation rate, respectively.

It is noted that all vector and contour plots shown are taken from the solution obtained with the standard k- $\epsilon$  turbulence model. They are primarily intended to give a qualitative insight into the flow in the region around the processing element.

- Figs. 12 - 13 Sketch of the downstream positions for the analysis of the different flow profiles.
- Fig. 14 Velocity profile in the first gap, at the downstream position  $x=0.413\text{m}$
- Fig. 15  $k$  profile in the first gap, at the downstream position  $x=0.413\text{m}$
- Fig. 16  $\epsilon$  profile in the first gap, at the downstream position  $x=0.413\text{m}$
- Fig. 17  $k$  profile, at the downstream position  $x=0.4136\text{m}$
- Fig. 18  $\epsilon$  profile, at the downstream position  $x=0.4136\text{m}$
- Fig. 19  $k$  profile, at the downstream position  $x=0.415\text{m}$
- Fig. 20  $\epsilon$  profile, at the downstream position  $x=0.415\text{m}$
- Fig. 21  $k$  profile in the second gap, at the downstream position  $x=0.423\text{m}$
- Fig. 22  $\epsilon$  profile in the second gap, at the downstream position  $x=0.423\text{m}$
- Fig. 23  $k$  profile, at the downstream position  $x=0.426\text{m}$
- Fig. 24  $\epsilon$  profile, at the downstream position  $x=0.426\text{m}$

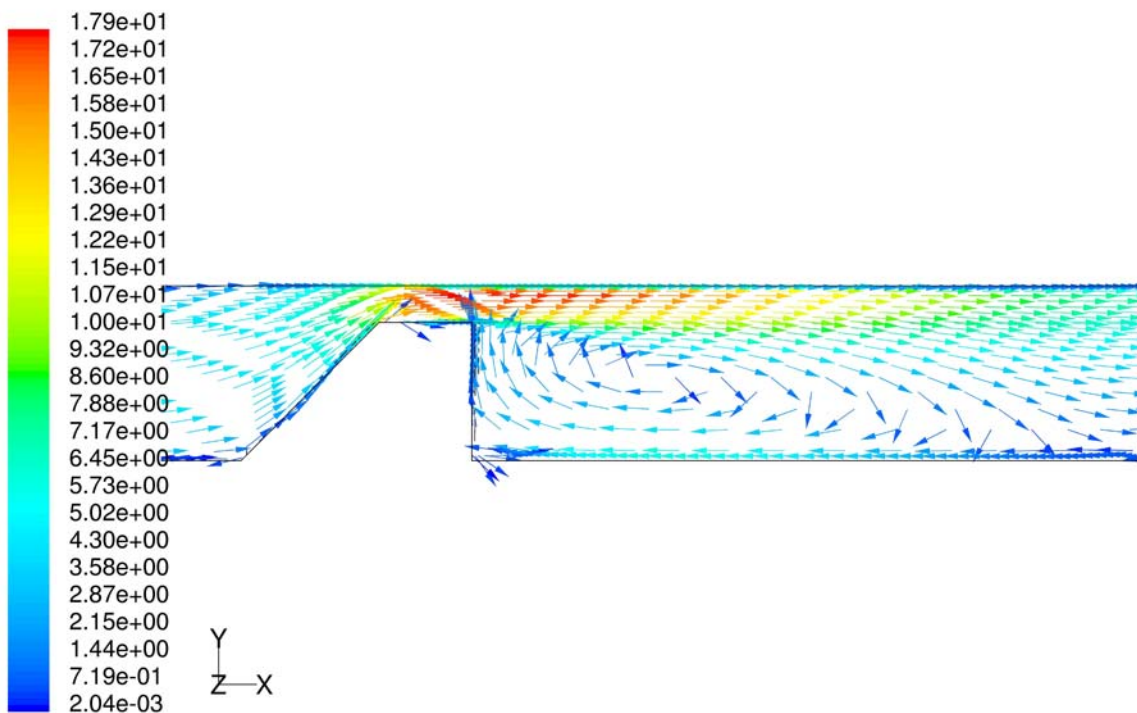


Figure 6: Velocity vectors colored by velocity magnitude (m/s), at the first gap.

As it is indicated by the strong recirculation zone in the wake of the gap, the backflow is significant in this region.

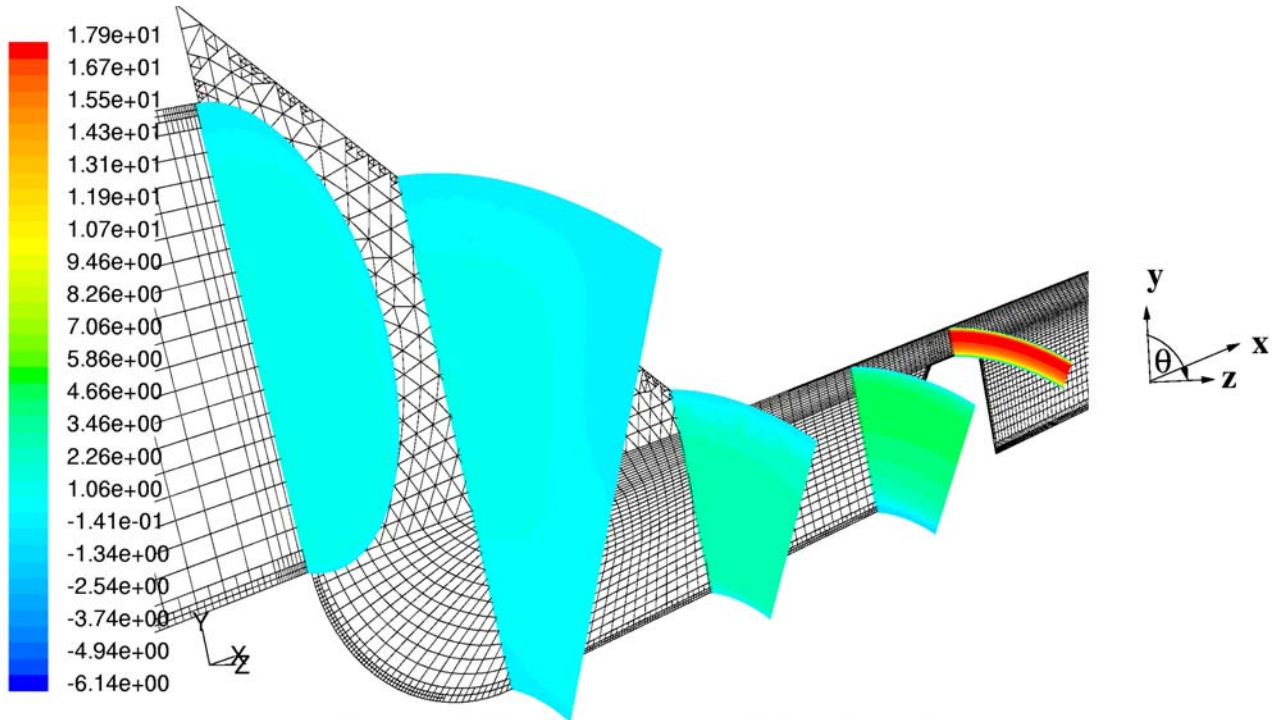


Figure 7: Contours of x velocity (m/s). Flow situation between the base plate of the processing element and the first gap.

It becomes evident that, right after the base plate of the processing element, the flow varies in the circumferential direction  $\theta$ , which is clearly to be expected. However, approaching the first narrow gap, the flow recovers quickly its circumferential homogeneity. Hence, the flow downstream from the first gap can be regarded as cylindrically symmetric.

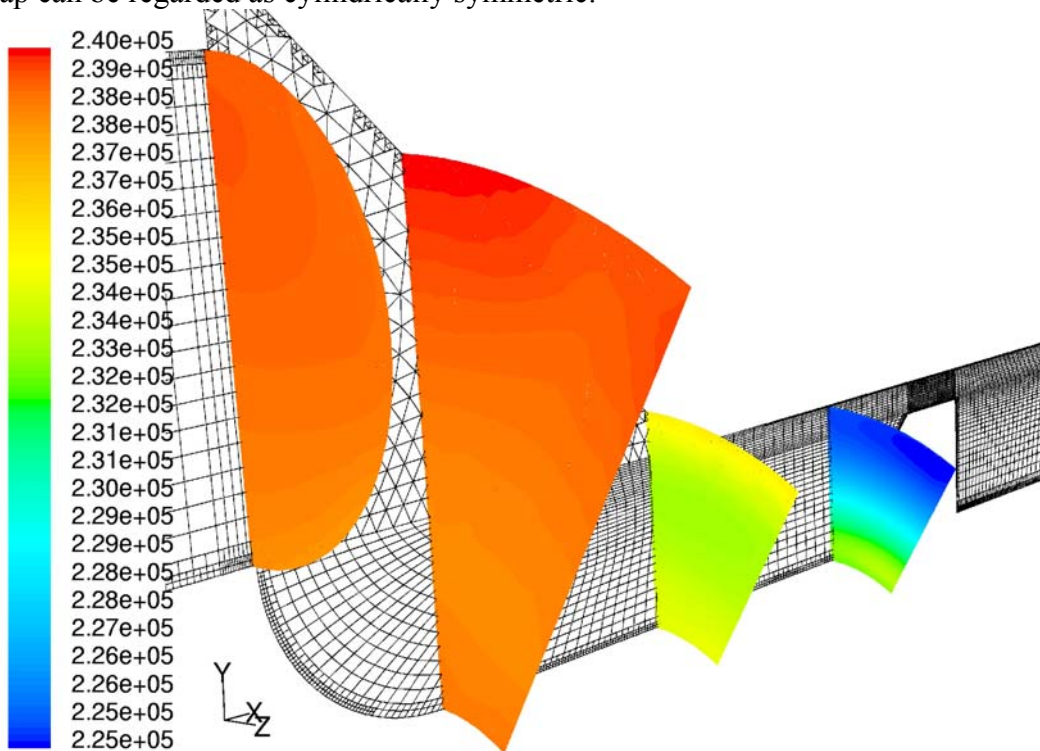


Figure 8: Contours of static pressure (Pa) at different locations downstream the base plate.



As already illustrated by the velocity contours in Figure 7, the recovery of the circumferential homogeneity is also shown by the fact that the isobars become concentric lines the closer they are to the gap.

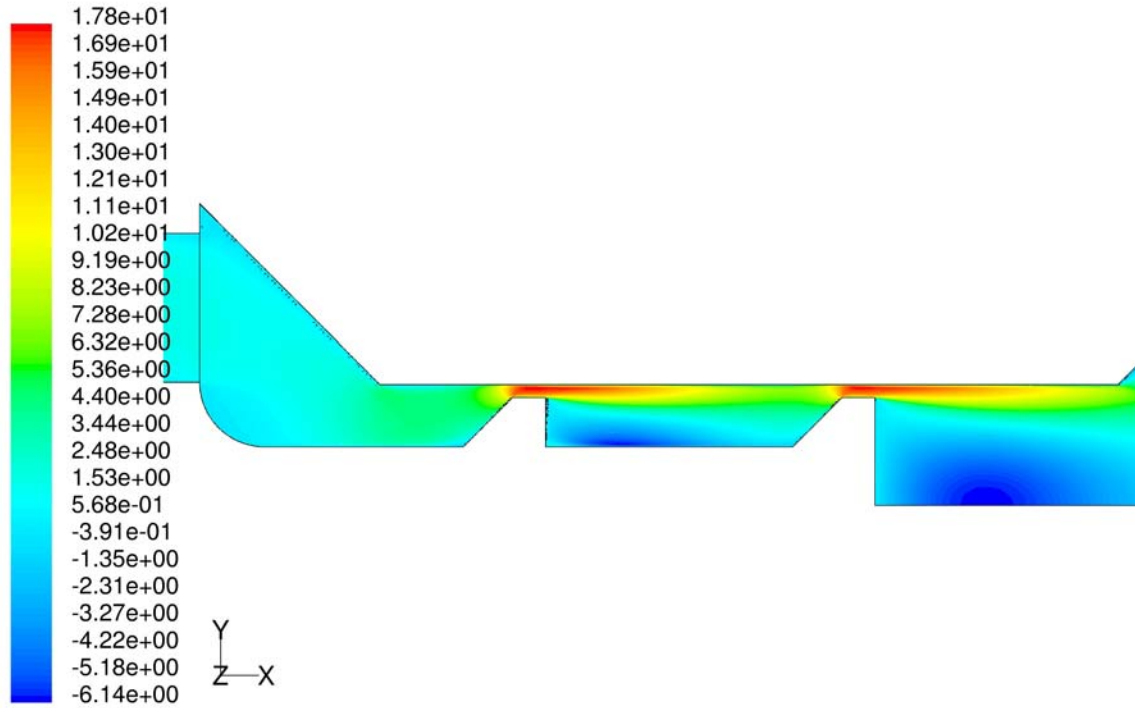


Figure 9: Contours of velocity component in the axial direction ( $v_x$  (m/s)).

The flow is strongly accelerated as it approaches the narrow gaps. Negative values denoted by dark blue areas indicate regions with strong backflow downstream from both gaps. The shown results are obtained using a standard  $k-\epsilon$  turbulence model with enhanced wall treatment.

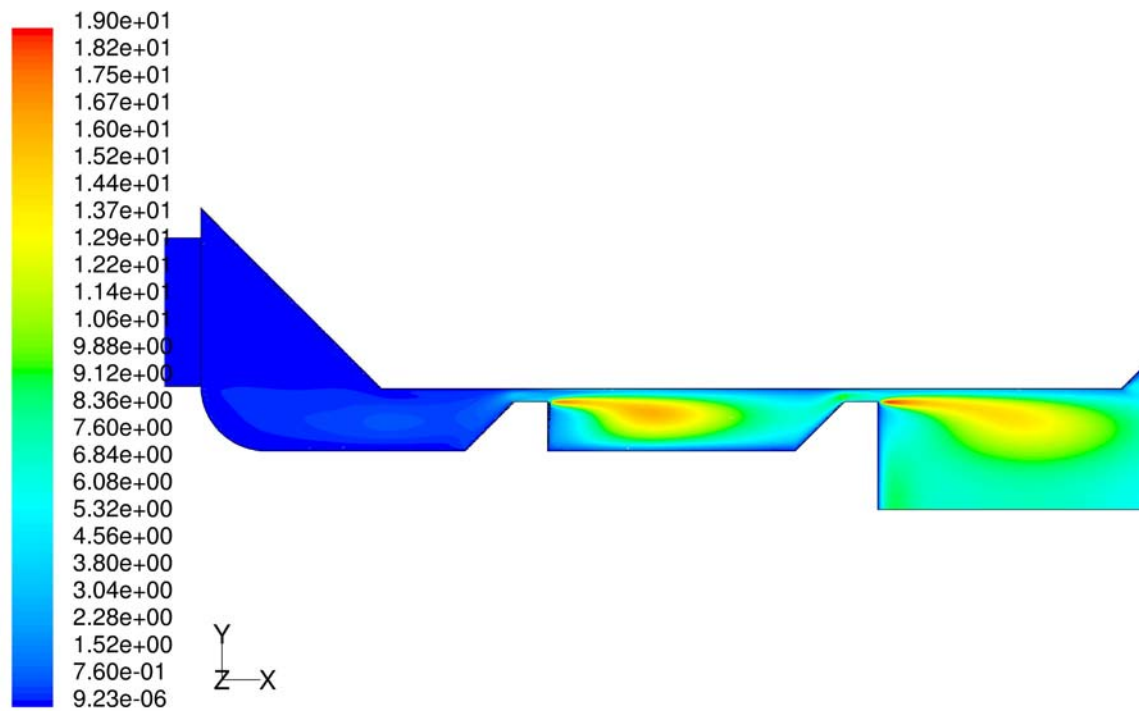


Figure 10: Contours of turbulent kinetic energy  $k$  ( $\text{m}^2/\text{s}^2$ ).

The strong shear-induced production of turbulence in the wakes after the rear edges of the gaps becomes evident. The turbulent kinetic energy reaches a maximum in these shear layers.

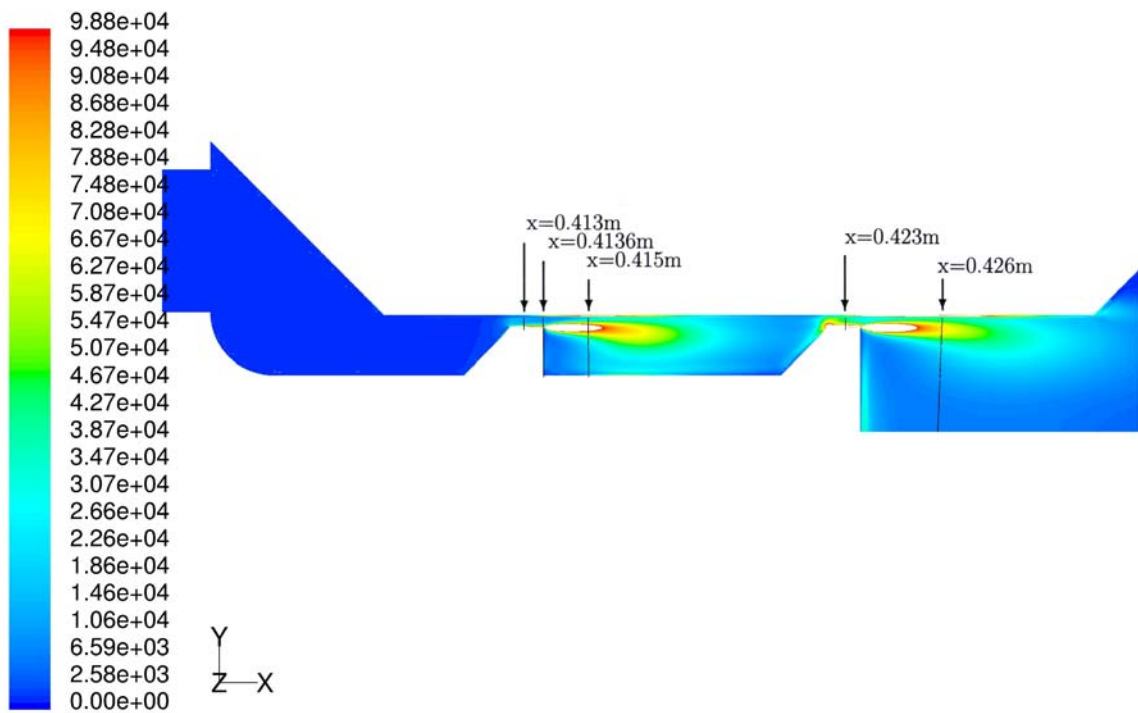


Figure 11: Contours of turbulent dissipation rate  $\epsilon$  ( $\text{m}^2/\text{s}^3$ ).

The maximum values of dissipation are reached in the regions, where the shear of the flow is highest. In order to get an appropriate color code it was necessary to clip the maximum values

beyond  $1 \cdot 10^5 \text{ (m}^2/\text{s}^3)$  near the backward facing edges of the processing element. The Figures 16, 18, 20, 22 and 24 will show the profiles for  $\varepsilon$  at the positions which are marked by the arrows in this contour plot. These diagrams will in particular reveal the maximum values of  $\varepsilon$  which are clipped here and appear as white areas.

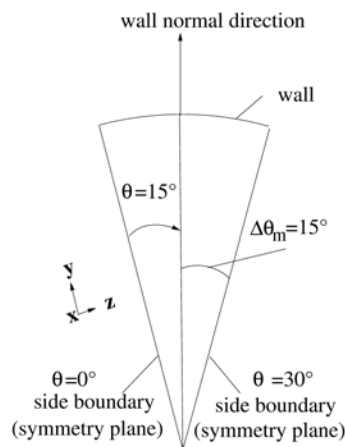


Figure 12: Circumferential position, i.e.,  $\theta=15^\circ$ , of the profiles shown in the Figures 14-24.

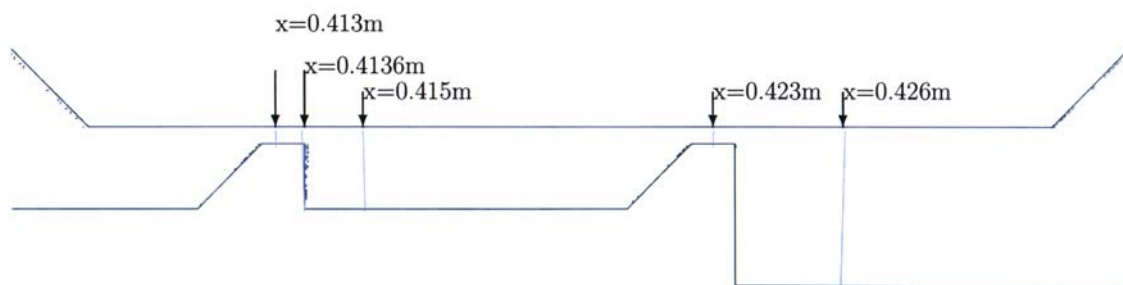


Figure 13: Downstream positions of the profiles shown in Figures 14-24.

Figures 12 and 13 show, respectively, the circumferential and downstream positions of the profiles shown in the Figures 14-24. In all these diagrams the profiles of the individual flow quantities are plotted vs. the wall normal direction shown in Figure 12.

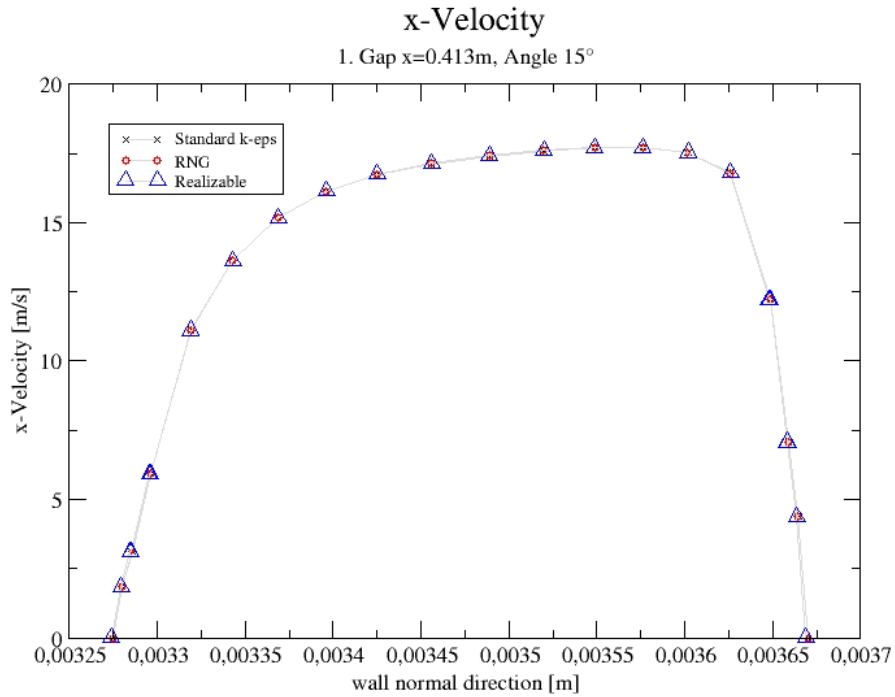


Figure 14: Streamwise velocity profiles over the height of the first gap.

The results achieved with the different  $k-\epsilon$  turbulence models with enhanced wall treatment show practically no difference. The maximum  $x$ -velocity over the gap-height is reached at a point beyond the center of the gap.

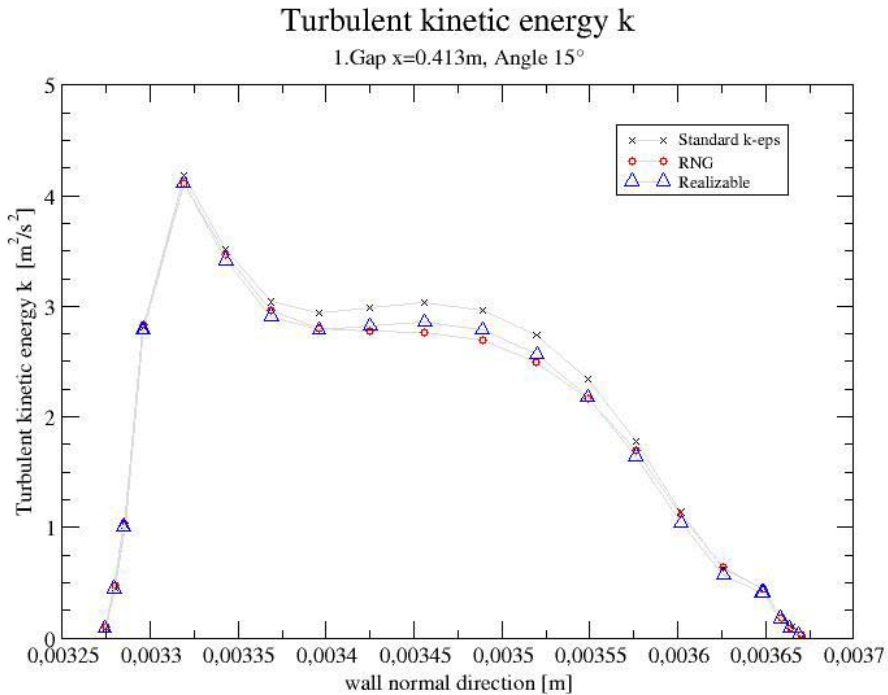


Figure 15: Profiles of the turbulent kinetic energy  $k$  over the height of the first gap at  $x=0.413\text{ m}$ .

The results obtained with the individual turbulence models show again no significant differences.

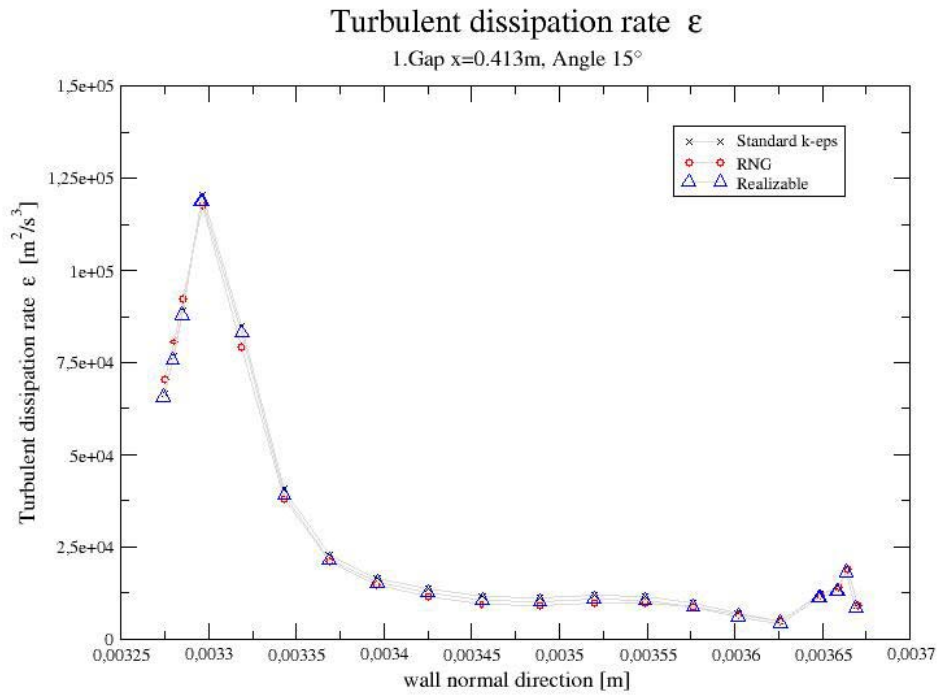


Figure 16: Profiles of the turbulent dissipation rate  $\epsilon$  inside the first gap at  $x=0.413\text{m}$ .

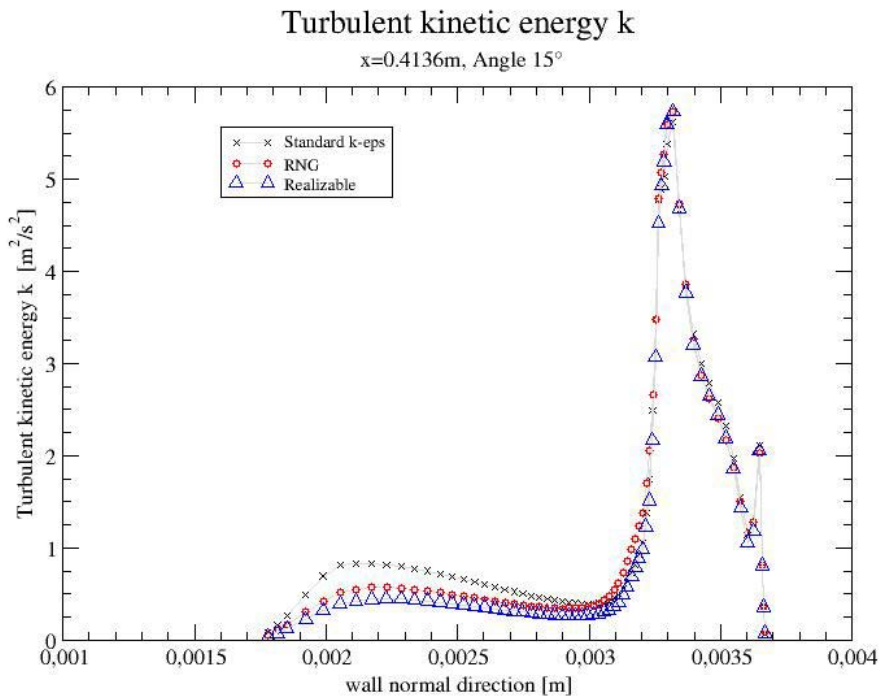


Figure 17: Profiles of the turbulent kinetic energy  $k$  immediately after the first gap at  $x=0.4136\text{m}$ .

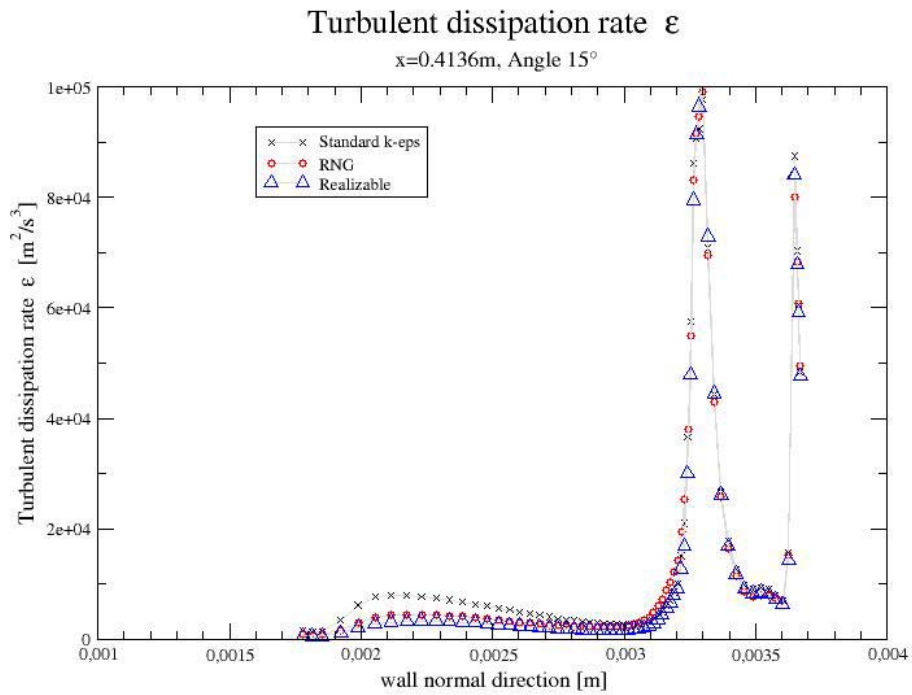


Figure 18: Profiles of the turbulent dissipation rate  $\epsilon$  immediately after the first gap at  $x=0.4136 \text{ m}$ .

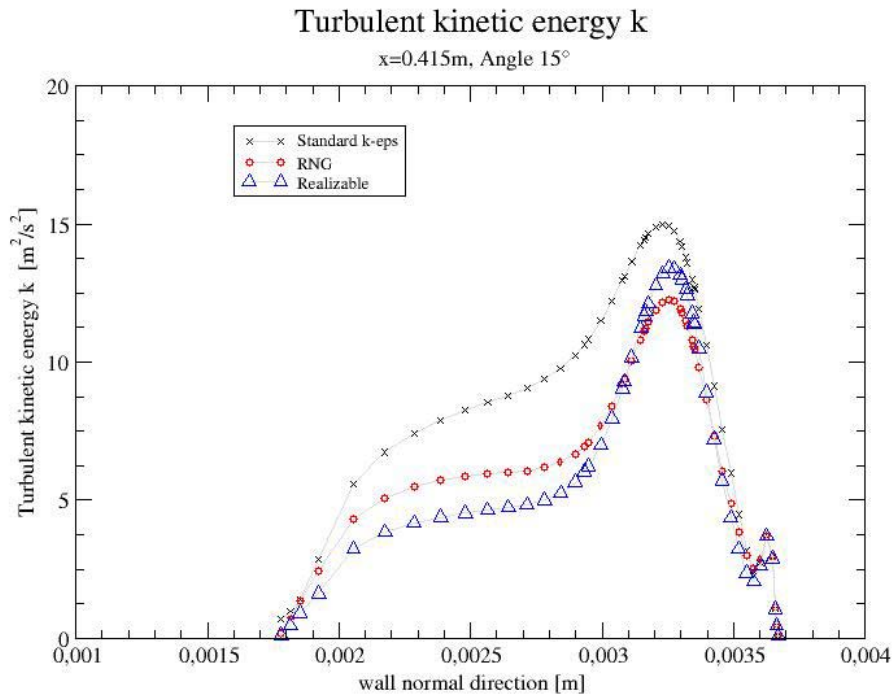


Figure 19: Profiles of the turbulent kinetic energy  $k$  in the wake after the first gap at  $x=0.415 \text{ m}$ .

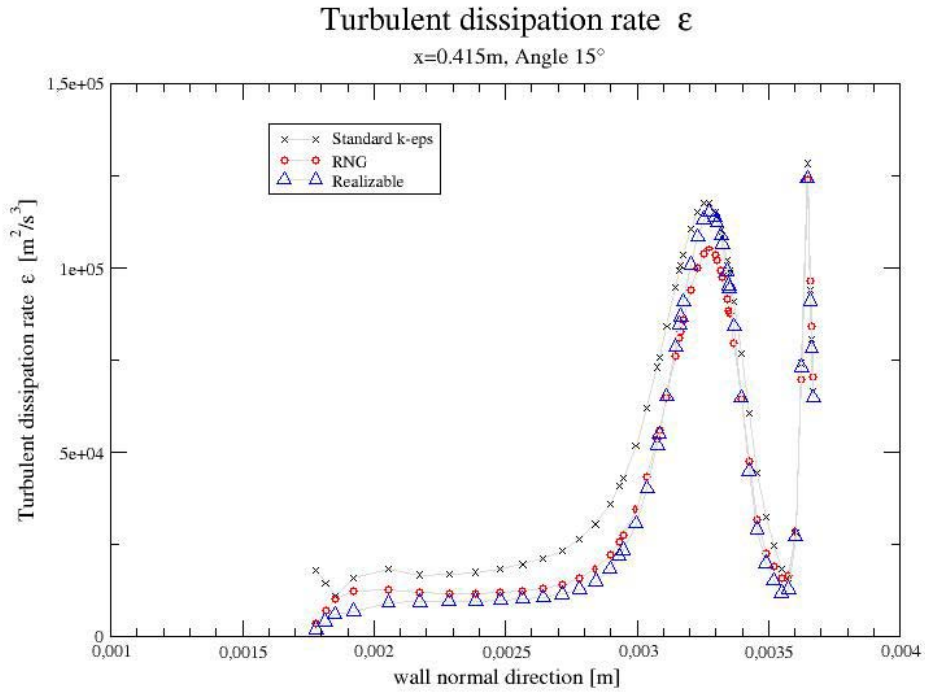


Figure 20: Profiles of the turbulent dissipation rate  $\epsilon$  in the wake after the first gap at  $x=0.415\text{m}$ .

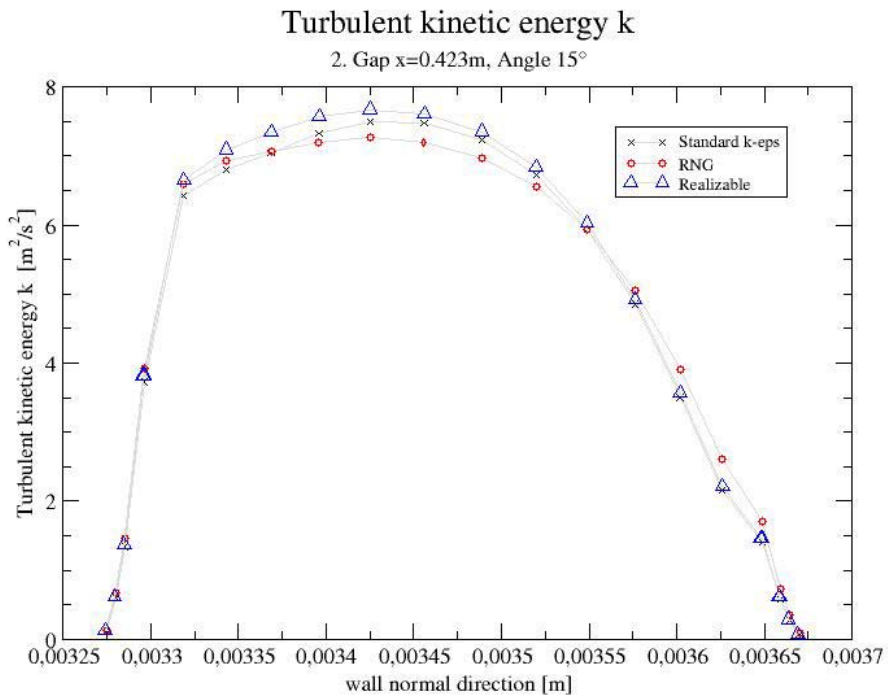


Figure 21: Profiles of the turbulent kinetic energy  $k$  inside the second gap at  $x=0.423\text{m}$ .

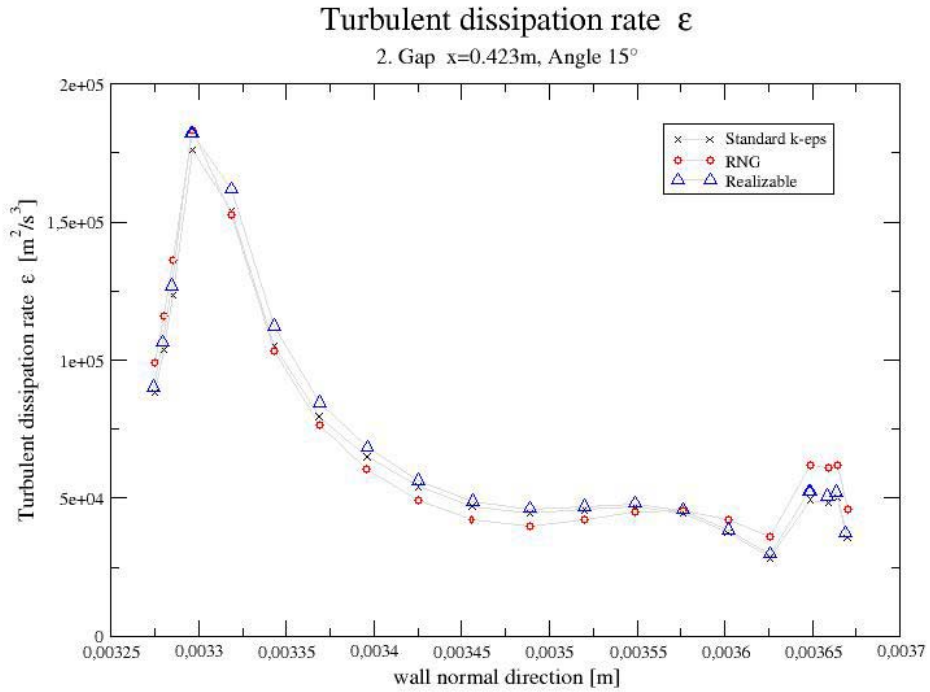


Figure 22: Profiles of the turbulent dissipation rate  $\epsilon$  inside the second gap at  $x=0.423\text{m}$ .

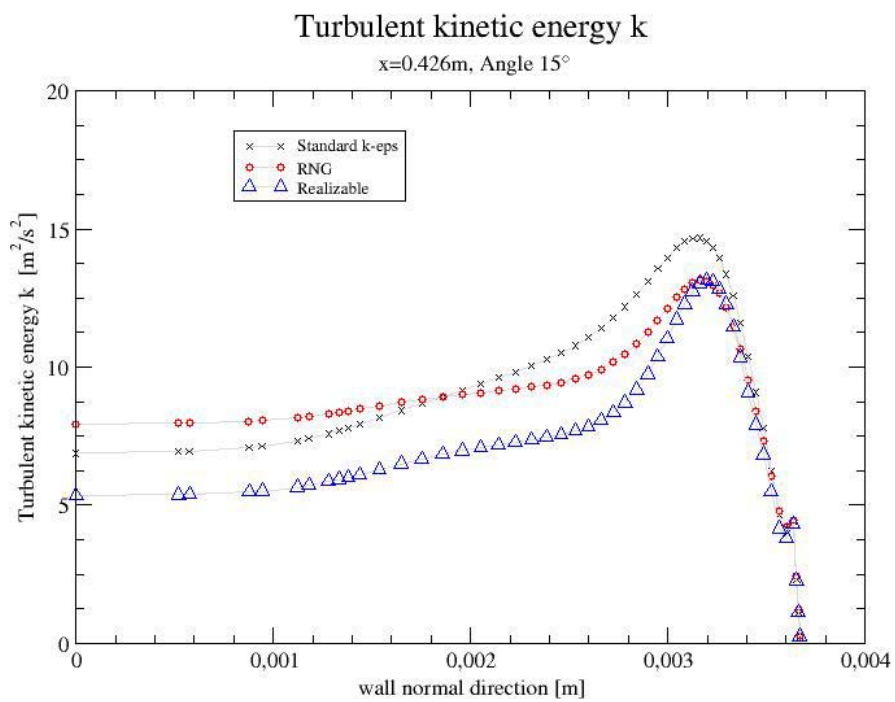


Figure 23: Profiles of the turbulent kinetic energy  $k$  in the wake after the second gap at  $x=0.426\text{m}$ .



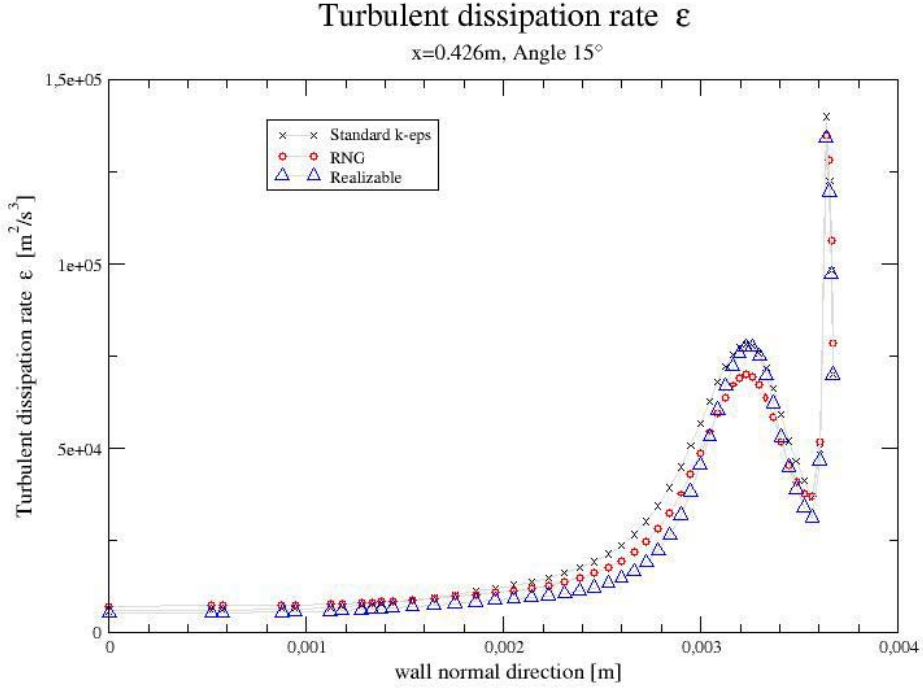


Figure 24: Profiles of the turbulent dissipation rate  $\varepsilon$  in the wake after the second gap at  $x=0.426\text{m}$ .

## 4 Estimation of the maximum drop-size based on the numerical results

Basic studies of droplet break-up in homogeneous and isotropic turbulent flow were first presented by Kolmogorov (1949) and Hinze (1955). The main assumption in these studies is that drop fragmentation is caused by dynamic pressure forces due to rapid turbulent fluctuations in the vicinity of the drops, which overcome the interfacial tension forces. This means that a) only velocity fluctuations over a distance close to the drop diameter are capable of causing large deformations and b) the turbulent eddies causing the deformation lie within the inertial subrange of the turbulent kinetic energy spectrum. Accordingly, an estimate of the maximum stable drop diameter  $d_{\max}$  can be obtained by equilibrating the inertial and the interfacial tension forces which is written as

$$\frac{\rho_c \delta u^2}{2} = \tilde{C} \frac{4\sigma}{d_{\max}} \quad \text{with } \tilde{C} = \text{const.} \quad (1)$$

Therein,  $\delta u^2$  denotes the mean-square velocity difference in the continuous phase over a distance equal to the drop diameter  $d_{\max}$ . Assuming an isotropic and homogeneous flow field and the diameter  $d_{\max}$  being much greater than the Kolmogorov length  $\eta$ ,

$$d_{\max} \gg \eta = \left( \frac{\nu_c^3}{\varepsilon} \right)^{1/4}, \quad (2)$$

the mean square velocity difference can be related to the distance  $d_{\max}$  as

$$\delta u^2 = 2(\varepsilon d_{\max})^{2/3} \quad (3)$$

depending only on the specific energy dissipation rate  $\varepsilon$ . Substituting eq. (3) into eq. (1) yields for the maximum stable drop diameter the relation

$$d_{\max} \left( \frac{\rho_c}{\sigma} \right)^{3/5} \varepsilon^{3/5} = C, \quad (4)$$

where the constant  $C=(We_{crit}/2)^{3/5}$  is given in terms of the critical Weber number  $We_{crit}$ , which has to be determined from experimental data. As a result the maximum stable drop diameter according to the Kolmogorov-Hinze theory reads

$$d_{\max} = \left( \frac{We_{crit}}{2} \right)^{3/5} \frac{\sigma^{3/5}}{\rho_c^{3/5} \varepsilon^{2/5}}. \quad (5)$$

In wall bounded flows the value for the dissipation rate  $\varepsilon$  needed in (5) can be roughly approximated based on correlations for the friction losses into the downstream direction. In the present consideration of the flow through the gap emulsifier the value for the energy dissipation rate  $\varepsilon$  can be obtained from the results of the numerical simulation described in the preceding sections. Besides the gain of a detailed insight into the flow field through the considered device the simulation was also motivated to provide an estimate for  $\varepsilon$ , which represents an essential input quantity into the droplet break-up modelling. Since the maximum stable droplet diameter is basically proportional to the inverse of  $\varepsilon$ , the region, where the highest dissipation rates are achieved, can be considered to be the relevant zone for the final distribution of the drop-size obtained in the outflow of the emulsifier.

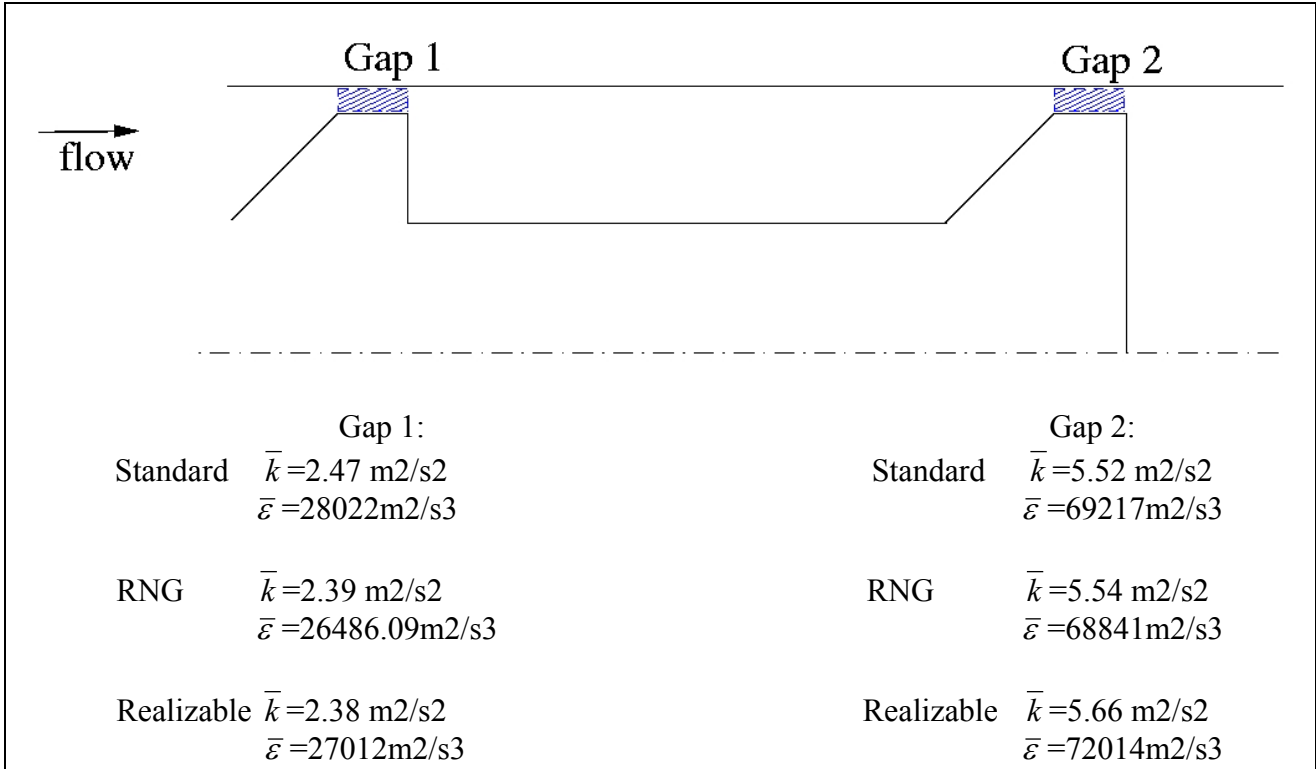


Figure 25: Cross-section of the annular gaps (shaded areas) and corresponding volumetric averages.

The numerical results for the present flow configuration show, that the dissipation rate exhibits the highest values in the second gap (see Figures 16, 18, 20, 22 and 24). Therefore, the mean dissipation rate obtained by averaging the numerical solution over the annular volume of the second gap is chosen as an appropriate input value for the estimation of the maximum droplet diameter in the present study. Figure 25 shows the cross-section of the annular volumes of the two gaps above

the processing element and the averages over the corresponding gap volumes for the dissipation rate and the turbulent kinetic energy. It becomes evident again that the alternatively applied turbulence models give not significantly different results.

Concerning the determination of the critical Weber number  $We_{crit}$  Karabelas (1978) derived for the case of turbulent continuous phase flow through a cylindrical pipe with diameter  $D$  the expression

$$We_{crit} = 5.9 \left( \frac{\rho_c D \bar{u}_c}{\mu_c} \right)^{-1/6} \quad (6)$$

Applying this dependence on the bulk flow Reynolds number of the continuous phase,  $Re_c = \rho_c \bar{u}_c D / \mu_c$ , to the present annular gap flow, where the hydraulic diameter  $D_h = d_a - d_i$  is the relevant diameter, the critical Weber is evaluated as  $We_{crit} = 1.235$ . Using this value for  $We_{crit}$  the maximum drop-size correlation according to the Kolmogorov-Hinze theory given by eq. (5) is rewritten as

$$d_{max} = 0.749 \frac{\sigma^{3/5}}{\rho_c^{3/5} \varepsilon^{2/5}} \quad (7)$$

It is noted that the Kolmogorov-Hinze relation (7) is strictly valid only for small differences in the molecular viscosities of the continuous and the dispersed phase. Davis (1985), therefore, extended this approach to cases, where the viscosity of the dispersed phase is significantly higher than that of the continuous phase, by adding a viscous force term, such that

$$d_{max} = \frac{K}{\rho_c^{3/5} \varepsilon^{2/5}} \left( \sigma + \frac{\mu_d \sqrt{2} (\varepsilon d_{max})^{1/3}}{4} \right)^{3/5} \quad (8)$$

Deviating from Davis' original suggestion, who set the constant  $K$  in (8) to be unity, the present consideration assumes for constant  $K$  the same functional dependence on the critical Weber number as for the constant  $C$  occurring in eq.(4). Setting the constant  $K = C = 0.748$  makes equation (8) approach the Kolmogorov-Hinze equation (7), if the viscosity of the dispersed phase is neglected.

#### 4.1 Comparison with experimental data

The Kolmogorov-Hinze correlation, eq.(7), as well as the extension due to Davis, eq.(8), were evaluated for three different test cases which have been investigated by Mrs. Tcholakova at the LCPE-Sofia in corresponding experiments with the gap emulsifier. In these experiments with water and soybean oil the resulting drop size distributions at the outflow of the device were measured for three different interfacial tensions  $\sigma$ . Their numerical values and those of all the other relevant parameters – these were in all three cases the same - are listed in Table 3. The continuous phase data always refer to the properties of water the dispersed phase data to those of soybean oil.

Case 1	Case 2	Case 3
$\sigma=10 \cdot 10^{-3}$ N/m	$\sigma=7 \cdot 10^{-3}$ N/m	$\sigma=3.8 \cdot 10^{-3}$ N/m
Gap width 395 $\mu$ m	Gap width 395 $\mu$ m	Gap width 395 $\mu$ m
$\dot{V}=0.13 \cdot 10^{-3}$ m <sup>3</sup> /s	$\dot{V}=0.13 \cdot 10^{-3}$ m <sup>3</sup> /s	$\dot{V}=0.13 \cdot 10^{-3}$ m <sup>3</sup> /s
$\rho_c=998$ kg/m <sup>3</sup>	$\rho_c=998$ kg/m <sup>3</sup>	$\rho_c=998$ kg/m <sup>3</sup>
$\mu_c=10^{-3}$ Pa s	$\mu_c=10^{-3}$ Pa s	$\mu_c=10^{-3}$ Pa s
$\rho_d=920$ kg/m <sup>3</sup>	$\rho_d=920$ kg/m <sup>3</sup>	$\rho_d=920$ kg/m <sup>3</sup>
$\mu_d=50 \cdot 10^{-3}$ Pa s	$\mu_d=50 \cdot 10^{-3}$ Pa s	$\mu_d=50 \cdot 10^{-3}$ Pa s

Table 3: Relevant parameters of the three test cases.

The measured drop size spectra for each case are shown as pdf-histograms and cumulated pdfs in the Figures 26-28. In the present consideration the maximum experimentally measured stable drop size is defined as the diameter which is exceeded by not more than 5% of the sample. It is denoted in the following by  $d_{95}$ .

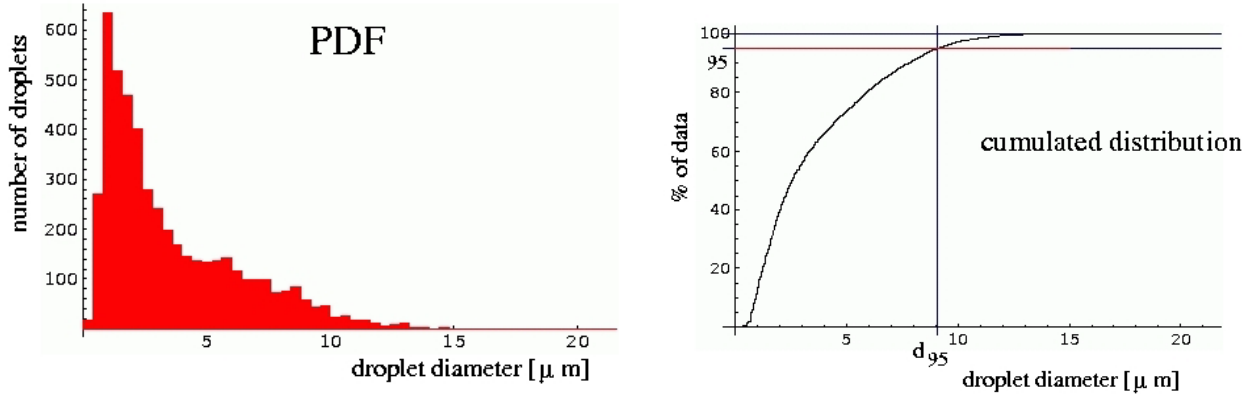


Figure 26: Case1,  $\sigma=10 \cdot 10^{-3}$  N/m,  $d_{95}=9.05 \mu\text{m}$ .

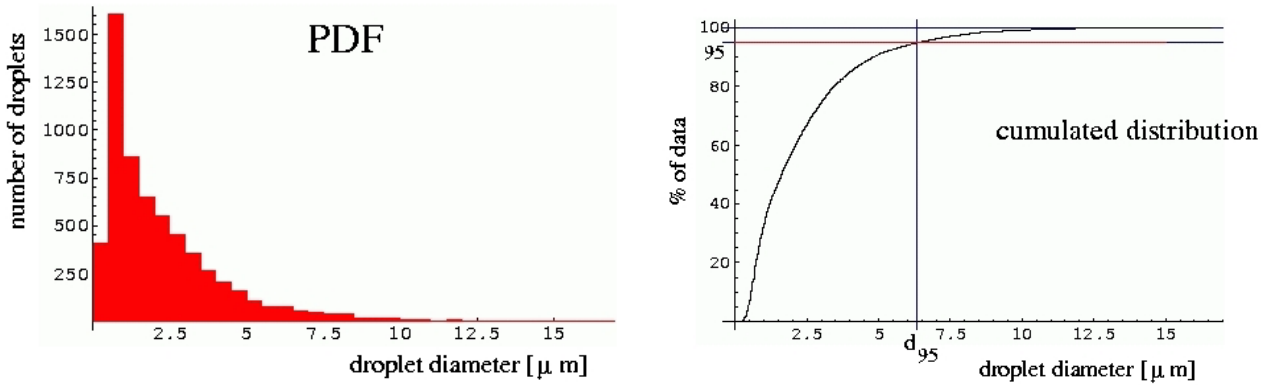


Figure 27: Case2,  $\sigma=7 \cdot 10^{-3}$  N/m,  $d_{95}=6.33 \mu\text{m}$ .

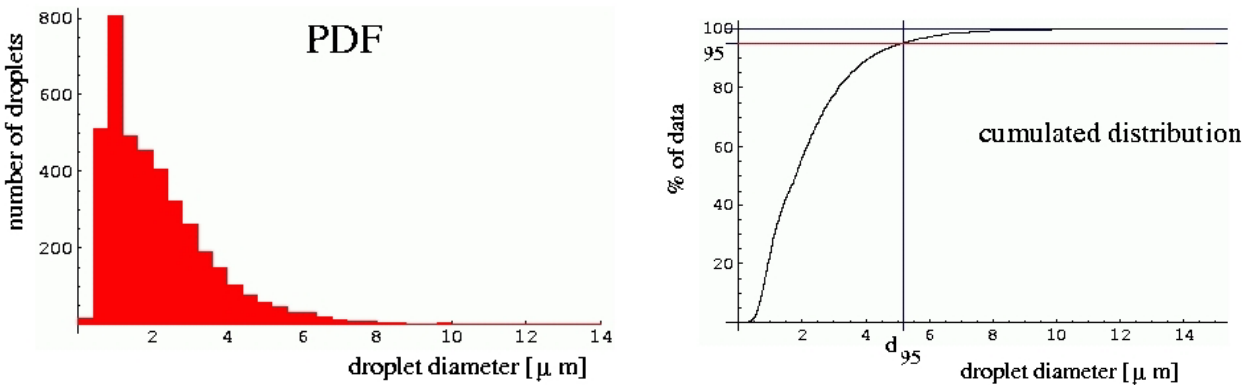


Figure 28: Case3,  $\sigma=3.8 \cdot 10^{-3}$  N/m,  $d_{95}= 5.17 \mu\text{m}$ .

The theoretical estimates, given by eq.(7) and eq.(8), respectively, use the dissipation rate field provided by the numerical simulation as input. For all three cases the solution obtained with the  $k-\varepsilon$  model is used to compute the volumetric average value in the second gap,  $\bar{\varepsilon} = 69217[\text{m}^2/\text{s}^3]$ , as shown in Figure 25.

The maximum drop sizes estimated with the two considered correlations are listed in Table 4 and compared with the corresponding experimental values  $d_{95}$ .

	Case 1	Case 2	Case 3
Kolmogorov-Hinze, eq.(7), $d_{max}$ [ $\mu\text{m}$ ]	8.68	7.01	4.86
Davis, eq.(8), $d_{max}$ [ $\mu\text{m}$ ]	16.24	15.01	13.6
Experiments, $d_{95}$ [ $\mu\text{m}$ ]	9.05	6.33	5.17

Table 4: Estimated maximum drop sizes and experimental data.

The Kolmogorov-Hinze correlation shows an unexpectedly good agreement with the experiments, although it completely neglects the large difference in the viscosity of the two phases ( $\mu_d = 50 \mu_c$ ). In contrast, the model extension proposed by Davis shows considerable over-predictions. The viscous term which is introduced on the RHS of eq.(8) appears to overestimate the effect of the viscous forces on the droplet break-up in the present cases.

## 5 Discussion and further work

The individual flow profiles obtained at the different downstream locations reveal that the turbulent kinetic energy is considerably low inside the first gap (Fig. 15). The maximum local turbulence intensity  $T = (\sqrt{2k/3})/\bar{u}$ , with  $\bar{u}$  being the magnitude of the local average velocity, is about 8 % there. The turbulent kinetic energy is strongly increased in the wake after the first gap due to the high shear-induced production leading to a peak value of  $k$  in the shear layer formed downstream from the backward facing edge (Fig. 19). Some part of the turbulence produced in this first wake zone is convected downstream into the second gap, and, hence, in comparison to the first gap a more than double maximum turbulence intensity ( $T \approx 20\%$ ) is achieved there (Fig. 21). In the wake further downstream, the turbulent kinetic energy is increased again in the shear layer after the rear face of the processing element. About the same peak values of  $k$  are achieved as in the first wake (Fig. 23). Similar to the turbulent kinetic energy, the dissipation rate  $\varepsilon$  occurring in the wakes after the gaps varies strongly with the wall normal direction. As shown in Figs. 20 and 24,  $\varepsilon$  exhibits a peak in the upper shear layer after the rear edges of the gaps.

It is noted that the numerical results obtained with the alternatively applied turbulence models show all the same tendencies. Quantitatively, the results do not differ significantly, either.

Moreover, the present simulation makes particularly evident that the turbulent kinetic energy as well as the turbulent dissipation rate are considerably increased from gap to gap. As shown in Figure 25 the dissipation rate averaged over the volume of the second gap exceeds significantly the corresponding value of the first gap. It can be expected that up to some limit a higher number of gaps followed by wakes will basically produce a strongly enhanced average turbulence and dissipation in the gap farthest downstream. Since the magnitude of the dissipation is essential for the droplet break-up mechanism according to the emulsification theory, the observed gap-to-gap increase of the achievable mean dissipation rate has to be considered in the determination of the optimum number of gaps of the processing element.

The estimation of the maximum drop size using the average dissipation rate evaluated with the numerical results in the second gap gave a surprisingly good agreement with experimental data for the simplest droplet-break-up model. Applying on the other hand a basically more advanced model, which also accounts for the viscous forces within the dispersed phase produced considerable over-

predictions. The agreement/disagreement of the estimates should not be misinterpreted in terms of the predictive capability of the applied models. Both approaches are strictly valid only for isotropic homogeneous turbulence, which is not the case in the considered flow through the narrow gaps being highly sheared and subject to strong wall effects. Additionally, in the light of the considerable spatial variations of the dissipation rate  $\varepsilon$  over the gap height, as shown in Figure 22, there is also some arbitrariness in the actual choice of the volumetric average value as an appropriate input into the model correlations. From this point of view the good agreement obtained with the simple model could be rather fortuitous.

It is finally noted that the drawn conclusions are basically made just for the present case with the two-gap-emulsifier. The sensitivity of the achievable dissipation rates to the gap width as well as to the number of gaps has certainly to be investigated in further simulations, varying the number of gaps as well as the gap width. These simulations will be carried out for the new designed planar emulsifier, where a series of computationally less costly two-dimensional computations might be possible.

## 6 Emulsification by liquid jet break-up in another viscous fluid

One technique which may be applied for forming emulsions is to form the drops of the disperse phase by break-up of a liquid jet immersed in the carrier fluid. The process that leads to the formation of drops is the instability of the jet against axisymmetric disturbances. The linear analyses of the stability of the viscous jet in another liquid of different viscosity and density presented by Tomotika (1935) and by Meister and Scheele (1967) are the basis for the present investigations.

Tomotika was the first to present a linear stability analysis of a viscous jet immersed in another viscous fluid. He starts his analysis from the conservation equations of mass and momentum for incompressible Newtonian fluids in cylindrical coordinates. Body forces are not considered in the momentum equations. The equations read

$$\text{mass:} \quad \frac{\partial u}{\partial r} + \frac{u}{r} + \frac{\partial w}{\partial z} = 0 \quad ,$$

$$\text{r momentum:} \quad \frac{\partial u}{\partial t} + u \frac{\partial u}{\partial r} + w \frac{\partial u}{\partial z} = -\frac{1}{\rho} \frac{\partial p}{\partial r} + \nu \left( \frac{\partial^2 u}{\partial r^2} + \frac{1}{r} \frac{\partial u}{\partial r} - \frac{u}{r^2} + \frac{\partial^2 u}{\partial z^2} \right)$$

$$\text{z momentum:} \quad \frac{\partial w}{\partial t} + u \frac{\partial w}{\partial r} + w \frac{\partial w}{\partial z} = -\frac{1}{\rho} \frac{\partial p}{\partial z} + \nu \left( \frac{\partial^2 w}{\partial r^2} + \frac{1}{r} \frac{\partial w}{\partial r} + \frac{\partial^2 w}{\partial z^2} \right) .$$

When the stream function  $\psi$  is introduced according to the definitions of the velocity components  $u$  and  $w$  in the radial and the axial ( $z$ ) directions, respectively, which read

$$u = \frac{1}{r} \frac{\partial \psi}{\partial z} \quad \text{and} \quad w = -\frac{1}{r} \frac{\partial \psi}{\partial r} ,$$

the continuity equation is satisfied automatically, and the momentum equations remain as two differential equations for the pressure and the stream function. Eliminating the pressure from these two equations leads to the final differential equation for the stream function

$$\left( \frac{\partial}{\partial t} + \frac{1}{r} \frac{\partial \psi}{\partial z} \frac{\partial}{\partial r} - \frac{1}{r} \frac{\partial \psi}{\partial r} \frac{\partial}{\partial z} - \frac{2}{r^2} \frac{\partial \psi}{\partial z} \right) D\psi = \nu D D \psi \quad ,$$

where the differential operator  $D$  is

$$D = \frac{\partial^2}{\partial r^2} - \frac{1}{r} \frac{\partial}{\partial r} + \frac{\partial^2}{\partial z^2} .$$

Assuming that the velocities occurring in this equation are small, such that their products and products with their derivatives are small of second order and may be neglected, Tomotika arrives at the final equation

$$\left( D - \frac{1}{v} \frac{\partial}{\partial t} \right) D\psi = 0$$

for the stream function of the problem. This equation is valid for both the fluid inside the liquid jet, and for the surrounding carrier fluid. Solutions of the equation may be the solutions  $\psi_1$  and  $\psi_2$  of the equations

$$D\psi_1 = 0 \quad \text{and} \quad D\psi_2 - \frac{1}{v} \frac{\partial \psi_2}{\partial t} = 0 .$$

In order to obtain wavelike solutions with a possibility to describe the temporal instability of the system, we make the ansatz

$$\psi_i = \phi_i(r) \cdot e^{i(\omega t + kz)} \quad \text{for } i=1, 2,$$

where the amplitude function  $\phi_i$  depends on the radial coordinate only and is to be determined by solving the respective differential equations. Introducing this formulation of  $\psi_i$  into the two differential equations for  $\psi_1$  and  $\psi_2$ , we obtain the two solutions for the amplitude functions

$$\begin{aligned} \phi_1 &= A_1 r I_1(kr) + B_1 r K_1(kr) \quad \text{and} \\ \phi_2 &= A_2 r I_1(lr) + B_2 r K_1(lr) \quad , \end{aligned}$$

where  $l^2 = k^2 + i\omega/v$ . The general solution of Tomotika's final differential equation is the sum of the two functions resulting from the separate solutions for  $\phi_i$  and the exponential function for the dependencies on  $t$  and  $z$ , i.e.

$$\psi = \psi_1 + \psi_2 = \left\{ [A_1 r I_1(kr) + B_1 r K_1(kr)] + [A_2 r I_1(lr) + B_2 r K_1(lr)] \right\} \cdot e^{i(\omega t + kz)} .$$

In this solution, which corresponds to Tomotika's final differential equation, one should keep in mind that no relative motion of the jet and the carrier fluids is assumed. The solution is therefore to be considered with care when deriving conclusions from them on the instability behaviour of liquids in processes like emulsification.

The general solution  $\psi$  of Tomotika's final differential equation is to be specialized for treating the inner and outer fluids, i.e. the jet and the carrier fluids, respectively. This is due to the fact that the modified Bessel functions occurring in the general solution tend to diverge either at zero or at infinite values of their arguments. The functions  $I$  diverge at infinity, the functions  $K$  at zero value of their arguments. These functions must therefore be excluded from the solutions for the outer and inner fluids, respectively. Denoting the solution for the inner fluid with a prime, we obtain

$$\begin{aligned} \psi' &= [A_1 r I_1(kr) + A_2 r I_1(l'r)] \cdot e^{i(\omega t + kz)} , \quad \text{where } l'^2 = k^2 + i\omega/v' , \quad \text{and} \\ \psi &= [B_1 r K_1(kr) + B_2 r K_1(lr)] \cdot e^{i(\omega t + kz)} , \quad \text{where } l^2 = k^2 + i\omega/v . \end{aligned}$$

These solutions are to be adapted to dynamic boundary conditions, which link the two fluids together. The conditions ensure that there is no slip at the interface (i.e. the velocity components  $u$  and  $w$  at the jet surface are the same for the two fluids), that the tangential stress is continuous across the interface, i.e. that

$$\mu' \left( \frac{\partial^2 \psi'}{\partial r^2} - \frac{1}{r} \frac{\partial \psi'}{\partial r} - \frac{\partial^2 \psi'}{\partial z^2} \right)_{r=a} = \mu \left( \frac{\partial^2 \psi}{\partial r^2} - \frac{1}{r} \frac{\partial \psi}{\partial r} - \frac{\partial^2 \psi}{\partial z^2} \right)_{r=a} ,$$

and that the radial stress across the interface differs due to the surface tension, i.e. that

$$\tau_{rr}|_{r=a} = \tau'_{rr}|_{r=a} + \frac{\sigma}{a^2} (k^2 a^2 - 1) \xi .$$

In the condition on the radial stress, the quantity  $\xi$  is the radial displacement, which is given by the equation  $\xi = \psi'|_{r=a} \cdot k/(\omega a)$ .

These boundary conditions establish four equations for the four unknown coefficients  $A_1$ ,  $A_2$ ,  $B_1$  and  $B_2$ . The system of equations is homogeneous in the coefficients. A non-trivial solution therefore exists only in the case that the coefficient determinant of the system vanishes. This leads to the solution of the problem in the form of the dispersion relation of the system, which, in contrast to the corresponding relations for the inviscid jet by Rayleigh and the viscous jet by Weber, is a determinantal equation. The dispersion relation reads

$$\begin{vmatrix} I_1(ka) & I_1(l'a) & K_1(ka) & K_1(la) \\ kaI_0(ka) & l'aI_0(l'a) & -kaK_0(ka) & -laK_0(la) \\ \frac{2\mu'}{\mu}k^2I_1(ka) & \frac{\mu'}{\mu}(k^2+l'^2)I_1(l'a) & 2k^2K_1(ka) & (k^2+l'^2)K_1(la) \\ F_1 & F_2 & F_3 & F_4 \end{vmatrix} = 0 ,$$

where the functions  $F_1$  through  $F_4$  are given by the expressions

$$F_1 = 2i\frac{\mu'}{\mu}k^2I_1'(ka) - \frac{\omega\rho'}{\mu}I_0(ka) + \frac{\sigma(k^2a^2-1)}{a^2}\frac{k}{\omega\mu}I_1(ka) ,$$

$$F_2 = 2i\frac{\mu'}{\mu}kl'I_1'(l'a) + \frac{\sigma(k^2a^2-1)}{a^2}\frac{k}{\omega\mu}I_1(l'a) ,$$

$$F_3 = 2ik^2K_1'(ka) + \frac{\omega\rho}{\mu}K_0(ka) , \text{ and}$$

$$F_4 = 2iklK_1'(la) .$$

Primes at the modified Bessel functions  $I$  and  $K$  indicate the derivative of the function with respect to its argument.

A further specialisation of the solution is now introduced in order to treat low flow velocities. This case is identified with negligible inertia of the two fluids, which corresponds to the case that the two densities  $\rho'$  and  $\rho$  vanish. In the limit of this case, we obtain a new form of the above determinant, which reads

$$\begin{vmatrix} I_1(ka) & kaI_1'(ka) & K_1(ka) & kaK_1'(ka) \\ I_0(ka) & I_0(ka) + kaI_1(ka) & -K_0(ka) & -K_0(ka) + kaK_1(ka) \\ \frac{\mu'}{\mu}I_1(ka) & \frac{\mu'}{\mu}kaI_0(ka) & K_1(ka) & -kaK_0(la) \\ G_1 & G_2 & K_1'(ka) & G_4 \end{vmatrix} = 0 ,$$

where the functions  $G_1$ ,  $G_2$  and  $G_4$  read

$$G_1 = \frac{\mu'}{\mu}I_1'(ka) + \frac{\sigma(k^2a^2-1)}{2i\omega a\mu}\frac{1}{ka}I_1(ka) ,$$



$$G_2 = \frac{\mu'}{\mu} \left[ I_1'(ka) + kaI_1''(ka) - I_0(ka) \right] + \frac{\sigma}{2i\omega a \mu} (k^2 a^2 - 1) I_1'(ka) \quad , \text{ and}$$

$$G_4 = K_1'(ka) + kaK_1''(ka) + K_0(ka) \quad .$$

The determinant can now be further simplified for the limiting cases that the viscosity ratio  $\mu'/\mu$  of the inner and outer fluids is very large or very small, i.e. for the cases of a viscous liquid jet in a gas and of a gas jet in a liquid. For a very large value of the viscosity ratio, the result obtained converges to the result of Rayleigh (1892). The case that the viscosity ratio is very small yields a similar result, but characterised by the functions  $K_0$  and  $K_1$  instead of  $I_0$  and  $I_1$ .

In the case that the viscosity ratio of the two fluids involved in the flow exhibits an intermediate value, the full determinant containing the functions  $G_i$  must be evaluated. For a special case of a lubrication oil injected into a syrup, which exhibits the value  $\mu'/\mu = 0.91$ , Taylor made experiments which may be considered in the light of the above theory. For this viscosity ratio, the above determinantal dispersion relation yields the maximum growth rate at the optimum wave number  $ka|_{\text{opt}} = 0.568$ . This is equivalent to the wavelength  $\lambda_{\text{opt}} = 5.53 \cdot 2a$ . In Taylor's experiments, the jet exhibited a radius of  $a = 0.272 \text{ mm}$ , and the inter-droplet distance in the region where the jet had broken down was  $3.452 \text{ mm}$ . This is equivalent to a non-dimensional wave number of  $ka = 2\pi a/\lambda = 0.5$ , which may be identified with the wave number of the fastest growing wave, since no control of the jet break-up was used to influence the disturbance wavelength. This experimental result may therefore be directly compared to the value of  $0.568$  from the theoretical prediction. The deviation is  $13.6\%$ , which is a relatively high value. One reason for this slight discrepancy may be seen in the fact that the theory does not account for the relative motion of the two fluids with a finite relative velocity, and in the simplification to disregard fluid inertia.

A more general description of the process was given by Meister and Scheele, who incorporated the relative motion in the theory. This theory will be transcribed into a form for use in the presently relevant work on liquid emulsification by means of jet injection into another liquid.

## References

- Davies, J.T., "Drop sizes of emulsions related to turbulent energy dissipation rates", *Chemical Engineering Science*, Vol. 40, No. 5, 839-842 (1985).
- Hinze, J. O., "Fundamentals of the Hydrodynamic Mechanism of Splitting in Dispersion Processes", *A.I.Ch.E. Journal*, Vol. 1, No. 3, 289-295 (1955)
- Karabelas, A.J., "Droplet Size Spectra Generated in Turbulent Pipe Flow of Dilute Liquid/Liquid Dispersions", *A.I.Ch.E. Journal*, Vol. 24, No. 2, 170-180 (1978)
- Kolmogorov, A. N., "On the Breaking of Drops in Turbulent Flow", *Doklady Akad. Nauk. U.S.S.R.*, Vol. 66, 82 (1949).
- B.J. Meister and G.F. Scheele: Generalized solution of the Tomotika stability analysis for a cylindrical jet. *AIChE J.* **13** (1967), 682-688.
- Lord Rayleigh, J.W.S.: On the instability of a cylinder of viscous liquid under capillary force. *Phil. Mag.* **34** (1892), 145-154.
- S. Tomotika: On the instability of a cylindrical thread of a viscous liquid surrounded by another viscous fluid. *Proc. R. Soc. London A* **150** (1935), 322-337.